coatings

MDPI

*Article*

# Hot-Corrosion Behavior of $Gd_2O_3$–$Yb_2O_3$ Co-Doped YSZ Thermal Barrier Coatings in the Presence of $V_2O_5$ Molten Salt

**Yang Li, Yajuan She and Kai Liao ***

School of Mechanical & Electrical Engineering, Hunan Applied Technology University, Changde 415000, China; liyang5862022@163.com (Y.L.); sheyajuan94@163.com (Y.S.)
* Correspondence: liaokai102@csuft.edu.cn

**Abstract:** In this study, thermal barrier coatings (TBC) consisting of 3.5 mol% $Yb_2O_3$-stabilized $ZrO_2$ co-doped with 1 mol% $Gd_2O_3$ and 1 mol% $Yb_2O_3$ (referred to as GdYb-YSZ) were fabricated by means of air plasma spraying. The as-fabricated coatings exhibited a metastable tetragonal ($t'$) structure. The hot-corrosion behavior of the GdYb–YSZ TBCs was investigated at 700, 800, 900, and 1000 °C for 10 h in the presence of $V_2O_5$ molten salt. During the corrosion tests, the $t'$ phase transformed into a monoclinic (m) phase; nevertheless, it was still detected on the corroded surfaces. The amount of $t'$ phase decreased with increasing corrosion temperature. The corrosion products formed on the GdYb-YSZ TBCs in $V_2O_5$ comprised Yb, Gd-doped $YVO_4$, and m-$ZrO_2$, irrespective of the temperature of corrosion. However, higher temperatures changed the morphologies of the Yb- and Gd-doped $YVO_4$ corrosion products. The GdYb–YSZ TBCs exhibited improved corrosion resistance to $V_2O_5$ molten salt when compared to YSZ TBCs, and the related mechanism is discussed in detail in this paper.

**Keywords:** thermal barrier coatings (TBCs); GdYb–YSZ; hot corrosion; $V_2O_5$; corrosion products



**Citation:** Li, Y.; She, Y.; Liao, K. Hot-Corrosion Behavior of $Gd_2O_3$–$Yb_2O_3$ Co-Doped YSZ Thermal Barrier Coatings in the Presence of $V_2O_5$ Molten Salt. *Coatings* **2023**, *13*, 886. https://doi.org/10.3390/coatings13050886

Academic Editor: Narottam P. Bansal

Received: 22 March 2023
Revised: 30 April 2023
Accepted: 2 May 2023
Published: 8 May 2023



## 1. Introduction

Thermal barrier coatings (TBCs) are widely applied on components of advanced gas-turbine engines, which are subjected to high temperatures, to provide thermal protection, thereby improving the efficiency and performance of the engines [1–5]. A common thermal barrier coating (TBC) consists of a ceramic topcoat and a bond coat. The ceramic topcoat typically contains 7–8 wt% $Y_2O_3$-stabilized $ZrO_2$ (YSZ), which possesses several desirable characteristics for TBC applications, including a high melting point, low thermal conductivity, thermal expansion coefficient similar to that of the substrate, and high toughness [1,6]. The most commonly used TBC fabrication technologies are air plasma spraying (APS), electron-beam physical vapor deposition, and plasma-spray physical vapor deposition [7–12]. The YSZ TBCs fabricated in their original state exhibit a desirable metastable tetragonal prime phase ($t'$), owing to their high toughness and suitability for TBC applications.

However, YSZ TBCs entail some limitations when used in gas-turbine engines [1,13–15]. At temperatures exceeding 1200 °C on the surface of TBCs, the $t'$ phase becomes unstable and breaks down into tetragonal (t) and cubic (c) phases. During cooling, the tetragonal phase undergoes a phase transformation to a monoclinic (m) phase. This is accompanied by a large volume expansion, which can crack and delaminate the coatings. Moreover, a high operation temperature accelerates the sintering of YSZ coatings, which is detrimental to the thermal insulation and thermal cycling behavior of TBCs. To achieve better thermal insulation, TBCs with low thermal conductivities are required. Several high-temperature ceramics, such as $ZrO_2$ doped/co-doped with rare-earth oxides, rare-earth zirconates, and rare-earth phosphates, which exhibit lower thermal conductivities than YSZ [16–21], have been proposed as potential candidates for TBC materials.

YSZ TBCs undergo severe degradation when operated in corrosive environments [22–28]. Impurities, such as vanadium, condense on the coating surface and melt at temperatures exceeding 700 °C, followed by their penetration into the coating. The Y in YSZ reacts with molten salt, resulting in a depletion of the stabilizer in the coating. As a result, an undesired phase transformation from the $t'$ phase to the m phase occurs in the coating. Researchers have made significant efforts to improve the corrosion resistance of YSZ coatings against vanadium. Studies have shown that doping YSZ with MgO and $Sc_2$ $O_3$ can enhance hot-corrosion resistance [29–32]. Furthermore, it has been reported that titania- or ceria-stabilized $ZrO_2$ exhibits better resistance to hot corrosion compared to YSZ [33,34]. Apart from YSZ, newly developed TBC candidates, such as rare-earth phosphates ($REPO_4$), have demonstrated excellent resistance to hot corrosion. In the presence of a molten salt ($V_2O_5$ or $V_2O_5$+$Na_2SO_4$), a solid solution of $RE(P,V)O_4$ can be formed, which is beneficial for maintaining the microstructural integrity of $REPO_4$ TBCs and enhancing the hot-corrosion resistance of these coatings [35].

Doping YSZ with rare-earth oxides can also improve hot-corrosion resistance. Guo et al. reported that $Gd_2O_3$–$Yb_2O_3$-co-doped YSZ (GdYb–YSZ) ceramics exhibited excellent resistance to molten-salt corrosion [36]. GdYb–YSZ has several desirable properties, such as low thermal conductivity, good phase stability, and high thermal expansion coefficient, making it a promising candidate for TBC applications [37]. However, previous research on molten-salt corrosion had focused only on ceramic pellets; the behavior of GdYb–YSZ TBCs in the presence of molten salt has not been studied so far.

The present study involves air plasma spraying (APS) of GdYb-YSZ TBCs and an investigation into their hot-corrosion characteristics when exposed to molten $V_2O_5$ at temperatures ranging from 700 to 1000 °C. The focus is on identifying the resulting corrosion products and tracking their microstructural evolution as the corrosion temperature increases. Additionally, the mechanism behind the formation of these corrosion products is discussed.

## 2. Experimental Procedures

To produce GdYb-YSZ powder with a chemical composition of 1 mol% Gd2O3 and 1 mol% Yb2O3 co-doped with 3.5 mol% $Y_2O_3$-stabilized $ZrO_2$, a chemical co-precipitation and calcination method was employed. The raw materials used were $RE_2O_3$ (RE = $Gd_2O_3$, $Yb_2$ O3, and $Y_2O_3$, purity 99.99%) and $ZrOCl_2{\cdot}8H_2O$ (purity 99.95%). The $RE_2O_3$ powders were first calcined at 900 °C for 4 h to eliminate moisture and other volatile impurities, and then dissolved in an appropriate amount of nitric acid. $ZrOCl_2{\cdot}8H_2O$ was dissolved in deionized water. The two solutions were mixed and stirred to obtain a homogeneous solution, which was then slowly added to excess ammonia water (pH > 12) to yield a precipitate. The precipitate was filtered and washed several times with distilled water and alcohol until the pH reached 7. The resulting precipitate was dried at 120 °C for 20 h and calcined at 800 °C for 5 h to achieve crystallization.

The obtained GdYb–YSZ powder was not suitable for direct thermal spraying because of its poor fluidity and agglomerated into microscopic particles when subjected to spray drying. The agglomerated GdYb–YSZ particles were sprayed onto Ni-based superalloy substrates with NiCoCrAlY as the bond coat through APS (Praxair 7700), obtaining a coating with thickness of about 200 μm. The chemical composition of NiCoCrAlY is provided in Table 1, and the spraying parameters selected from the pre-optimization procedures are listed in Table 2.

**Table 1.** The chemical composition of NiCoCrAlY bond coat.

| Element | Ni | Co | Cr | Al | Y |
|---|---|---|---|---|---|
| Content | Bal. | 20–22 | 24 | 20 | 1.5 |

**Table 2.** Air plasma spraying parameters for GdYb–YSZ TBCs.

| Parameter | NiCoCrAlY | GYb–YSZ |
|---|---|---|
| Current (A) | 530 | 600 |
| Voltage (V) | 50 | 56 |
| Primary gas, Ar (L/min) | 40 | 40 |
| Secondary gas, $H_2$ (L/min) | 10 | 10 |
| Feedstock giving rate (g/min) | 30 | 30 |
| Spray distance (mm) | 100 | 100 |

Hot-corrosion tests were carried out by subjecting the salt-covered GdYb-YSZ coatings to $V_2O_5$ at a concentration of 10 mg/cm$^2$, followed by heating them at temperatures of 700, 800, 900, and 1000 °C for a duration of 10 h. After the completion of heating, the furnace was cooled to room temperature. The phase structures of both the as-fabricated and corroded surfaces of the coatings were determined using X-ray diffraction (XRD) with a Rigaku Diffractometer (Tokyo, Japan), while microstructural and compositional analyses were conducted using a scanning electron microscope (SEM; TDCLS4800, Hitachi Ltd., Tokyo, Japan) equipped with energy-dispersive spectroscopy (EDS, IE 350).

## 3. Results and Discussion

Figure 1 shows the SEM image of the YSZ agglomerated particles after thermal spraying. The particles exhibit a spherical shape with sizes ranging from 30 to 50 μm. The XRD patterns of the as-sprayed and corroded GdYb–YSZ coatings are presented in Figure 2. The as-sprayed coating has a $t'$ phase structure, which is desirable for TBC applications owing to its high toughness. Following 10 h of hot corrosion at 700 °C, the XRD pattern of the sample still reveals the presence of the $t'$ phase peaks, albeit with reduced intensity and broadening. Notably, the appearance of the (111) and (−111) peaks corresponding to the m phase at approximately $2\theta \approx 28$ and 31° indicates $t'$-phase decomposition during the corrosion process. Additionally, a few strong peaks resembling YVO4 (PDF#17-0341) with slight angle shifts are evident, implying the dissolution of other elements. At higher corrosion temperatures of 800, 900, and 1000 °C, the XRD patterns of all samples exhibit similar characteristics, with discernible peaks corresponding to the $t'$, m, and doped-$YVO_4$ phases. Notably, the relative intensity of the m phase increases with higher temperatures, signifying an increase in the formation of the m phase. The XRD analysis indicates that corrosion temperature has a minimal effect on the type of corrosion products formed; however, it does affect their relative abundance. Even though our study used an excessive amount of molten salt, the presence of the $t'$ phase in the corroded coating surfaces suggests that the GdYb-YSZ coating may maintain its phase stability and demonstrate some resistance to hot corrosion.

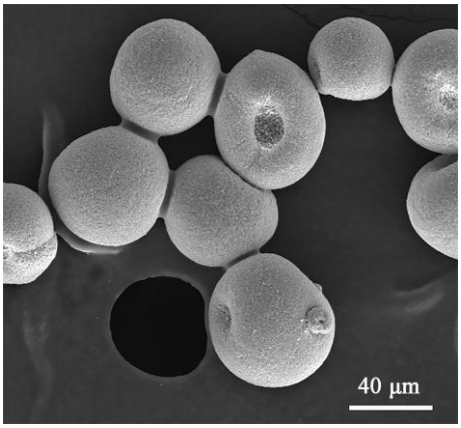


**Figure 1.** SEM micrographs of GdYb–YSZ agglomerated particles.

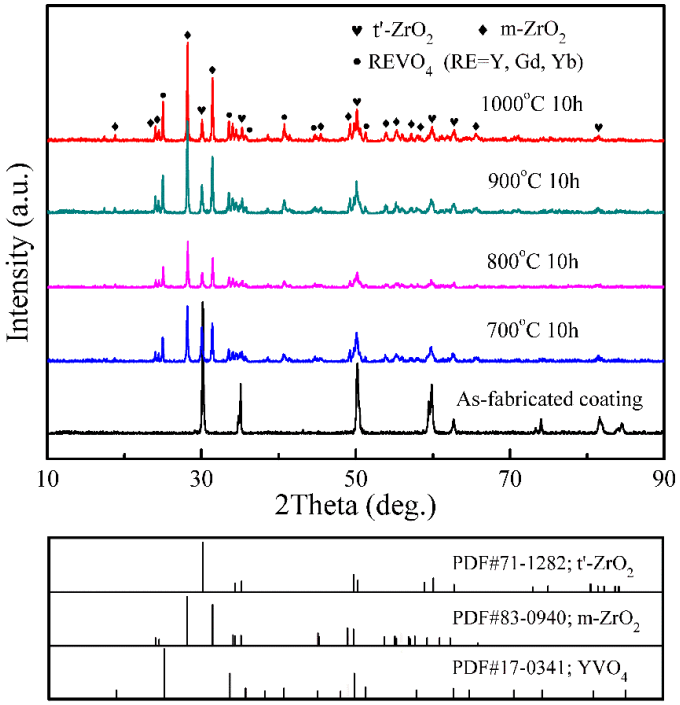


**Figure 2.** XRD patterns of the as-sprayed and corroded GdYb–YSZ coatings exposed to $V_2O_5$ molten salt at 700, 800, 900, and 1000 °C for 10 h. The standard PDF cards of m-$ZrO_2$, $t'$-$ZrO_2$, and $YVO_4$ are also presented (bottom figure).

Phase instability is one of the key factors causing the failure of $ZrO_2$-based TBCs [33,38]. According to the XRD analysis, the GdYb–YSZ coatings exhibit phase decomposition during the corrosion tests. In order to assess the hot-corrosion resistance of the coatings, we calculated the amount of m phase present in the samples after hot corrosion, which allowed us to estimate the degree of $t'$-phase decomposition. The equations used for this calculation are as follows:

$$\frac{M_m}{M_{t'}} = 0.82\frac{I_m(\bar{1}11) + I_m(111)}{I_{t'}(111)} \quad (1)$$

$$M_m + M_{t'} = 1 \quad (2)$$

In these equations, the variables used in the calculation are defined as follows: $M_m$ and $M_{t'}$ represent the mole fractions of the $m$ and $t'$ phases, respectively, and $I$ corresponds to the integral intensity of the diffraction peaks. The results of the calculations are presented in Figure 3, where it is evident that higher corrosion temperatures cause an increase in the m-phase content and a decrease in the $t'$-phase content. According to the analysis, as the hot-corrosion temperature increases from 700 to 1000 °C, the mole fraction of the m-phase content in the coating increases from 68.87 to 85.32 mol%.

After 10 h of exposure to hot corrosion at 700 °C, the GdYb-YSZ coating exhibits a typical surface morphology, as shown in Figure 4a. Compared to the as-sprayed coating, the corroded coating exhibits a distinct surface morphology. The surface of the coating appears to be entirely covered by the corrosion products. At a higher magnification using SEM (Figure 4b), it can be observed that the products possess bulk shape (A) and spherical shape (B). Table 2 lists the results of the EDS analysis used to determine the compositions of the products. Product A was found to contain Y, Gd, Yb, V, and O, while product B consists of Zr, O, and some rare-earth elements. Additional analysis reveals that A is composed of Yb- and Gd-doped $YVO_4$, whereas B contains $ZrO_2$ with some rare-earth elements. This is confirmed by the earlier XRD results, which identify the m-$ZrO_2$ phase

from the rare-earth content. Region C was also characterized using EDS and was found to contain more rare-earth elements than region B. Combined with the XRD results, it can be confirmed that region C corresponds to the sprayed coating, which has suffered little attack from the molten salt.

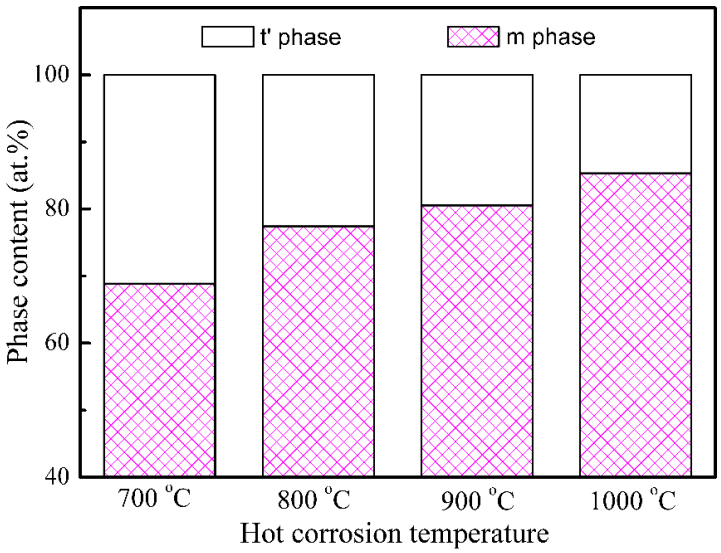


**Figure 3.** Calculated concentrations of m and $t'$ phases in GdYb–YSZ coatings after hot corrosion at 700, 800, 900, and 1000 °C for 10 h.

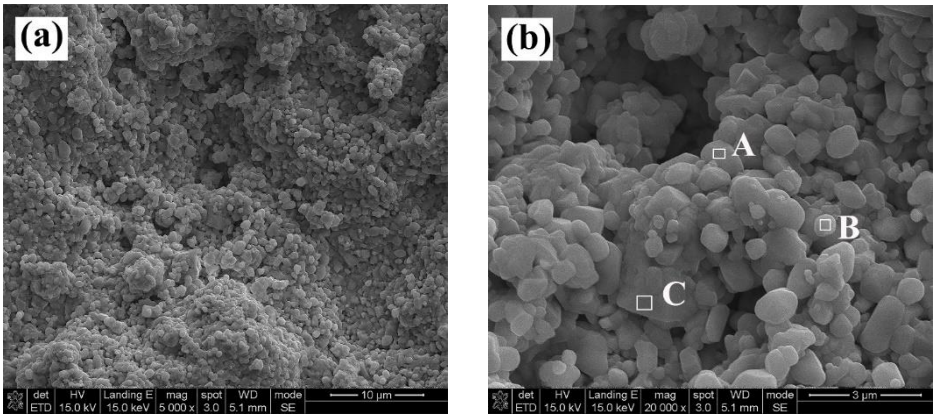


**Figure 4.** Surface morphology (**a**) and its enlarged image (**b**) of the GdYb–YSZ coating after hot corrosion in $V_2O_5$ molten salt at 700 °C for 10 h.

Figure 5 displays the SEM images of the GdYb-YSZ coating that has undergone hot corrosion for 10 h at 800 °C. The coating surface displays visible corrosion products. Figure 5b presents an enlarged image of the surface, where corrosion products with bulk and spherical shapes are clearly visible and labeled as D and E, respectively. The Yb- and Gd-doped $YVO_4$ and m-$ZrO_2$ compounds were identified through the EDS analysis and XRD findings, as shown in Table 3. As shown in Figure 5b, some as-sprayed coatings can be observed, as marked by F. This indicates that, under this corrosion condition, the coating surface is not completely corroded, suggesting some resistance to molten-salt corrosion.

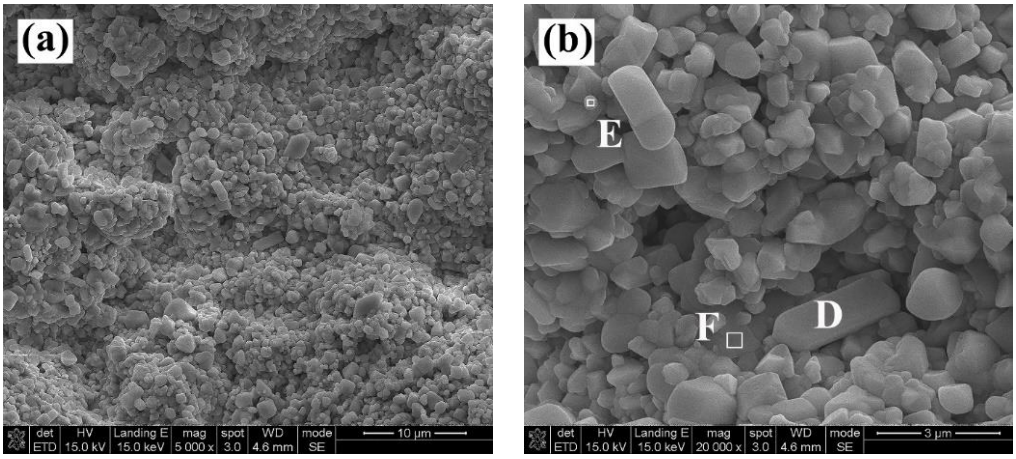


**Figure 5.** Surface morphology (**a**) and its enlarged image (**b**) of the GdYb–YSZ coating after hot corrosion in $V_2O_5$ molten salt at 800 °C for 10 h.

**Table 3.** Chemical compositions of regions A–J in Figures 4–7 (in at.%).

| | Y | Yb | Gd | Zr | V | O |
|---|---|---|---|---|---|---|
| A | 16.3 | 1.1 | 1.2 | — | 21.1 | 60.3 |
| B | 2.0 | — | 0.6 | 46.6 | — | 51.8 |
| C | 2.3 | 1.1 | 0.8 | 46.4 | — | 49.4 |
| D | 16.4 | 1.1 | 1.4 | — | 20.7 | 60.4 |
| E | 1.9 | — | 0.6 | 47.9 | — | 49.6 |
| F | 2.5 | 0.9 | 0.8 | 45.4 | — | 50.4 |
| G | 16.0 | 0.9 | 1.0 | — | 19.8 | 62.3 |
| H | 2.1 | — | 0.7 | 49.3 | — | 47.9 |
| I | 17.1 | 1.4 | 2.0 | — | 22.6 | 56.9 |
| J | 1.9 | — | 0.8 | 48.4 | — | 48.9 |

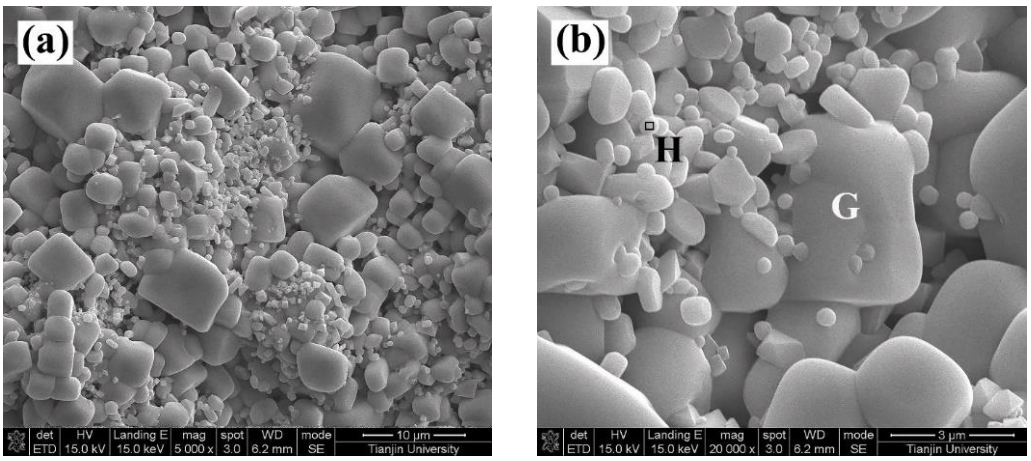


**Figure 6.** Surface morphology (**a**) and its enlarged image (**b**) of the GdYb–YSZ coating after hot corrosion in $V_2O_5$ molten salt at 900 °C for 10 h.

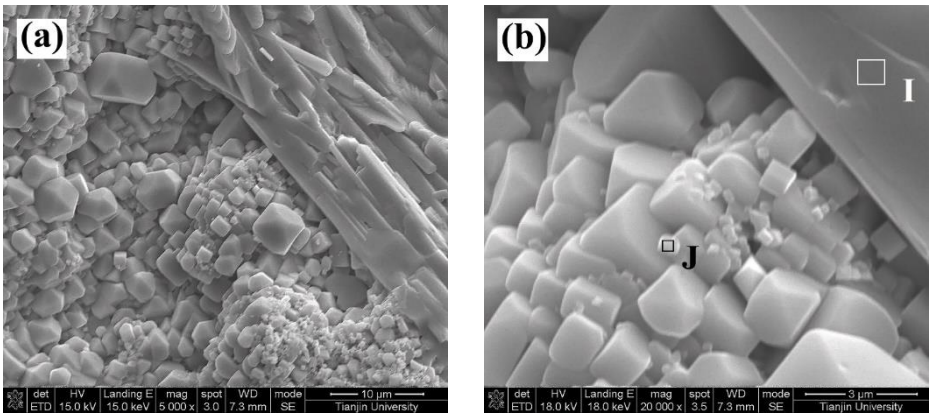


**Figure 7.** Surface morphology (**a**) and its enlarged image (**b**) of the GdYb–YSZ coating after hot corrosion in $V_2O_5$ molten salt at 1000 °C for 10 h.

The corrosion products form a continuous layer on the coating surfaces after 10 h of $V_2O_5$ corrosion at 900 and 1000 °C, as shown in Figures 6 and 7. The bulk-shaped crystals (G) are larger and later become rod-shaped (I), as shown in Figure 7. The EDS and XRD results show that compounds G and I are both Yb- and Gd-doped $YVO_4$. Meanwhile, spherical corrosion products are also observed in Figures 6 and 7, which are confirmed as m-$ZrO_2$ based on the above analysis. The study suggests that the type of corrosion products is not significantly affected by an increase in corrosion temperature; however, higher temperatures change the morphologies of the corrosion products of Yb- and Gd-doped $YVO_4$.

Previous studies have shown that YSZ coatings have poor resistance to $V_2O_5$ corrosion due to the $V_2O_3$ stabilizer's tendency to react with $V_2O_5$, leading to the depletion of Y and the decomposition of the desirable $t'$ phase. The formation of the m phase due to $V_2O_5$ attack could result in large stress and cracks in the coatings, which is detrimental for the thermal cycling performance of the coatings [22,24,25,39]. Despite being susceptible to $V_2O_5$ attack, the GdYb-YSZ coating exhibits a certain degree of hot-corrosion resistance, as confirmed by the presence of the $t'$ phase on the corroded surface even after 10 h of corrosion at 1000 °C. This suggests that the coating could retain its phase stability and may still display some resistance to hot corrosion.

The analysis conducted on the corrosion products of GdYb-YSZ coatings allowed us to describe the corrosion mechanism of the coating using the following equation:

$$V_2O_5(l) + GdYb - YSZ(s) \rightarrow (Y,\ Yb,\ Gd)VO_4(s) + m - ZrO_2(s) \quad (3)$$

The reason behind the superior corrosion resistance of GdYb-YSZ coatings when compared to YSZ coatings can be explained by the Lewis acid–base mechanism. According to this mechanism, acidic $V_2O_5$ reacts more easily with oxides having a higher basicity [40]. GdYb–YSZ coatings contain more rare-earth elements than YSZ coatings. Moreover, $Yb_2O_3$ has a lower basicity than $Y_2O_3$ and $Gd_2O_3$ [41,42]. Thus, some rare-earth elements, such as Yb, can remain in the coating as stabilizers when coming in contact with molten salt. Therefore, when molten salt is present, GdYb–YSZ coatings have a higher possibility of maintaining the $t'$-phase stability than YSZ coatings. However, GdYb–YSZ coatings still have hot-corrosion issues that require special attention.

## 4. Conclusions

In this study, GdYb-YSZ TBCs fabricated using APS were examined for their hot-corrosion behavior when subjected to $V_2O_5$ molten salt at 700–1000 °C for 10 h, and the following conclusions could be drawn:

(1) The GdYb-YSZ TBCs experienced some degree of attack by $V_2O_5$, but they showed better corrosion resistance compared to YSZ TBCs. This improved resistance can be attributed to the higher rare-earth content and lower basicity of $Yb_2O_3$.
(2) The as-fabricated GdYb-YSZ TBCs contained $t'$ phase, and even after hot corrosion, the $t'$ phase was still detectable on the corroded surfaces, indicating that the coatings had a certain level of resistance to phase decomposition. As the temperature of corrosion increased, the quantity of $t'$ phase decreased, while the amount of m phase increased.
(3) In addition to the m phase, Yb- and Gd-doped $YVO_4$ were generated as the corrosion products of the GdYb-YSZ TBCs in $V_2O_5$. Higher temperatures had no effect on the type of corrosion products but changed the morphologies of Yb- and Gd-doped $YVO_4$ crystals.

**Author Contributions:** Conceptualization and supervision, K.L.; validation and writing—original draft preparation, Y.L.; investigation and data curation, Y.S. All authors have read and agreed to the published version of the manuscript.

**Funding:** This study was sponsored by the Hunan Provincial Department of Education General Project, grant number 14C0766.

**Institutional Review Board Statement:** Not applicable.

**Informed Consent Statement:** Not applicable.

**Data Availability Statement:** Not applicable.

**Conflicts of Interest:** The authors declare no conflict of interest.

## References

1. Vaßen, R.; Jarligo, M.O.; Steinke, T.; Mack, D.E.; Stöver, D. Overview on advanced thermal barrier coatings. *Surf. Coat. Technol.* **2010**, *205*, 938–942. [CrossRef]
2. Yang, S.J.; Song, W.J.; Dingwell, D.B.; He, J.; Guo, H.B. Surface roughness affects metastable non-wetting behavior of silicate melts on thermal barrier coatings. *Rare Met.* **2022**, *41*, 469–481. [CrossRef]
3. Guo, L.; Gao, Y.; Ye, F.X.; Zhang, X.M. CMAS corrosion behavior and protection method of thermal barrier coatings for aeroengine. *Acta Metall. Sin.* **2021**, *57*, 1184–1198.
4. Yang, J.; Bai, S.; Sun, J.; Wu, H.; Sun, S.; Wang, S.; Li, Y.; Ma, W.; Tang, X.; Xu, D. Microstructural understanding of the oxidation and inter-diffusion behavior of Cr-coated Alloy 800H in supercritical water. *Corros. Sci.* **2023**, *211*, 110910. [CrossRef]
5. Yang, J.; Shang, L.; Sun, J.; Bai, S.; Wang, S.; Liu, J.; Yun, D.; Ma, D. Restraining the Cr-Zr interdiffusion of Cr-coated Zr alloys in high temperature environment: A Cr/CrN/Cr coating approach. *Corros. Sci.* **2023**, *214*, 111015. [CrossRef]
6. Xue, Z.L.; Guo, H.B.; Gong, S.K.; Xu, H.B. Novel ceramic materials for thermal barrier coatings. *J. Aeronaut. Mater.* **2018**, *38*, 10–20.
7. Xu, Z.H.; Zhou, X.; Wang, K.; Dai, J.W.; He, L.M. Thermal barrier coatings of new rare-earth composite oxide by EB-PVD. *J. Alloys Compd.* **2014**, *587*, 126–132. [CrossRef]
8. Liu, Y.; Ravichandran, R.; Chen, K.Y.; Patnaik, P. Application of machine learning to solid particle erosion of APS-TBC and EB-PVD TBC at elevated temperatures. *Coatings* **2021**, *11*, 11070845. [CrossRef]
9. Xie, Z.H.; Liu, Q.; Lee, K.I.; Zhu, W.; Wu, L.T.; Wu, R.T. The effect of bond coat roughness on the cmas hot corrosion resistance of EB-PVD thermal barrier coatings. *Coatings* **2022**, *12*, 12050596. [CrossRef]
10. Guo, Y.Q.; Wei, L.L.; He, Q.; Deng, Y.P.; He, W.T.; Guo, H.B. PS−PVD alumina overlayer on thermal barrier coatings against CMAS attack. *J. Therm. Spray Techn.* **2021**, *30*, 864–872. [CrossRef]
11. Guo, Y.Q.; Song, W.J.; Guo, L.; Li, X.X.; He, W.T.; Yan, X.D.; Dingwell, D.B.; Guo, H.B. Molten-volcanic-ash-phobic thermal barrier coating based on biomimetic structure. *Adv. Sci.* **2023**, *10*, 2205156. [CrossRef]
12. Guo, Y.Q.; Guo, L.; Li, X.X.; Jiang, C.Y.; Wei, L.L.; Zhu, X.Y.; Liu, D.R.; Song, W.J.; Dingwell, D.B.; Guo, H.B. Ultrafast laser reconstructed PS-PVD thermal barrier coatings with superior silicophobic triple-scale micro/nano structure. *Mater. Des.* **2023**, *228*, 111846. [CrossRef]
13. Loghman-Estarki, M.R.; Shoja Razavi, R.S.; Edris, H.; Pourbafrany, M.; Jamali, H.; Ghasemi, R. Life time of new SYSZ thermal barrier coatings produced by plasma spraying method under thermal shock test and high temperature treatment. *Ceram. Int.* **2014**, *40*, 1405–1414. [CrossRef]
14. Tsipas, S.A. Effect of dopants on the phase stability of zirconia-based plasma sprayed thermal barrier coatings. *J. Eur. Ceram. Soc.* **2010**, *30*, 61–72. [CrossRef]

15. Zhang, X.M.; Xin, H.; Guo, L. Crystallization behavior of calcium–magnesium–alumina–silicate coupled with NaCl/$Na_2SO_4$. *Corros. Commun.* **2023**, *10*, 1–9. [CrossRef]
16. Wang, Y.X.; Zhou, C.G. Microstructure and thermal properties of nanostructured gadolinia doped yttria-stabilized zirconia thermal barrier coatings produced by air plasma spraying. *Ceram. Int.* **2016**, *42*, 13047–13052. [CrossRef]
17. Wei, X.D.; Hou, G.L.; An, Y.L.; Yang, P.; Zhao, X.Q.; Zhou, H.D.; Chen, J.M. Effect of doping $CeO_2$ and $Sc_2O_3$ on structure, thermal properties and sintering resistance of YSZ. *Ceram. Int.* **2021**, *47*, 6875–6883. [CrossRef]
18. Liu, Z.G.; Zhang, W.H.; Ouyang, J.H.; Zhou, Y. Novel thermal barrier coatings based on rare-earth zirconates/YSZ double-ceramic-layer system deposited by plasma spraying. *J. Alloys Compd.* **2015**, *647*, 438–444. [CrossRef]
19. Wang, Y.H.; Ma, Z.; Liu, L.; Liu, Y.B. Reaction products of $Sm_2Zr_2O_7$ with calcium-magnesium-aluminum-silicate (CMAS) and their evolution. *J. Adv. Ceram.* **2021**, *10*, 1389–1397. [CrossRef]
20. Guo, L.; Li, B.W.; Cheng, Y.X.; Wang, L. Composition optimization, high-temperature stability, and thermal cycling performance of Sc-doped $Gd_2Zr_2O_7$ thermal barrier coatings: Theoretical and experimental studies. *J. Adv. Ceram.* **2022**, *11*, 454–469. [CrossRef]
21. Guo, L.; Yan, Z.; Li, Z.H.; Yu, J.X.; Wang, Q.; Li, M.Z.; Ye, F.X. $GdPO_4$ as a novel candidate for thermal barrier coating applications at elevated temperatures. *Surf. Coat. Technol.* **2018**, *349*, 400–406. [CrossRef]
22. She, Y.J.; Guo, Y.W.; Tan, Z.X.; Liao, K. $Na_2SO_4$ + $V_2O_5$ Corrosion behavior of $BaNd_2Ti_3O_{10}$ for thermal barrier coating applications. *Coatings* **2020**, *10*, 901. [CrossRef]
23. Huang, H.; Liu, C.; Ni, L.Y.; Zhou, C.G. Evaluation of microstructural evolution of thermal barrier coatings exposed to $Na_2SO_4$ using impedance spectroscopy. *Corros. Sci.* **2011**, *53*, 1369–1374. [CrossRef]
24. Liu, Z.G.; Ouyang, J.H.; Zhou, Y.; Zhu, R.X. Hot corrosion of $V_2O_5$-coated $NdMgAl_{11}O_{19}$ ceramic in air at 950 °C. *J. Eur. Ceram. Soc.* **2013**, *33*, 1975–1979. [CrossRef]
25. Yin, Y.C.; Ma, W.; Jin, X.L.; Li, X.Y.; Bai, Y.; Jia, R.L.; Dong, H.Y. Hot corrosion behavior of the $La_2(Zr_{0.7}Ce_{0.3})_2O_7$ ceramic in molten $V_2O_5$ and a $Na_2SO_4$+$V_2O_5$ salt mixture. *J. Alloys Compd.* **2016**, *689*, 123–129. [CrossRef]
26. Chen, X.L.; Sun, Y.W.; Chen, D.X.; Li, J.; Li, W.; Zeng, D.H.; Wu, D.L.; Zou, B.L.; Cao, X.Q. A comparative investigation on the corrosion degradation of plasma sprayed YSZ and $LnMgAl_{11}O_{19}$ (Ln = Nd, Sm, Gd) coatings exposed to the molten $V_2O_5$ + $Na_2SO_4$ salt mixture at 1100 °C. *J. Eur. Ceram. Soc.* **2019**, *39*, 3778–3787. [CrossRef]
27. Rahmatnezhad, K.; Zarastvand, M.R.; Talebitooti, R. Mechanism study and power transmission feature of acoustically stimulated and thermally loaded composite shell structures with double curvature. *Compos. Struct.* **2021**, *276*, 114557. [CrossRef]
28. Talebitooti, R.; Gohari, H.D.; Zarastvand, M.R. Multi objective optimization of sound transmission across laminated composite cylindrical shell lined with porous core investigating Non-dominated Sorting Genetic Algorithm. *Aerosp. Sci. Technol.* **2017**, *69*, 269–280. [CrossRef]
29. Bajpai, P.; Das, A.; Bhattacharya, P.; Madayi, S.; Kulkarni, K.; Omar, S. Hot corrosion of stabilized zirconia thermal barrier coatings and the role of Mg inhibitor. *J. Am. Ceram. Soc.* **2015**, *98*, 2655–2661. [CrossRef]
30. Loghman-Estarki, M.R.; Nejati, M.; Edris, H.; Shoja Razavi, R.S.; Jamali, H.; Pakseresht, A.H. Evaluation of hot corrosion behavior of plasma sprayed Scandia and yttria co-stabilized nanostructured thermal barrier coatings in the presence of molten sulfate and vanadate salt. *J. Eur. Ceram. Soc.* **2015**, *35*, 693–702. [CrossRef]
31. Liu, H.F.; Xiong, X.; Li, X.B.; Wang, Y.L. Hot corrosion behavior of $Sc_2O_3$-$Y_2O_3$-$ZrO_2$ thermal barrier coatings in presence of $Na_2SO_4$ + $V_2O_5$ molten salt. *Corros. Sci.* **2014**, *85*, 87–93. [CrossRef]
32. Loghman-Estarki, M.R.; Shoja Razavi, R.S.; Edris, H.; Bakhshi, S.R.; Nejati, M.; Jamali, H. Comparison of hot corrosion behavior of nanostructured ScYSZ and YSZ thermal barrier coatings. *Ceram. Int.* **2016**, *42*, 7432–7439. [CrossRef]
33. Habibi, M.H.; Guo, S.M. The hot corrosion behavior of plasma sprayed zirconia coatings stabilized with yttria, ceria, and titania in sodium sulfate and vanadium oxide. *Mater. Corros.* **2015**, *66*, 270–277. [CrossRef]
34. Hajizadeh-Oghaz, M.; Razavi, R.S.; Ghasemi, A.; Valefi, Z. $Na_2SO_4$ and $V_2O_5$ molten salts corrosion resistance of plasma-sprayed nanostructured ceria and yttria co-stabilized zirconia thermal barrier coatings. *Ceram. Int.* **2016**, *42*, 5433–5446. [CrossRef]
35. Guo, L.; Zhang, C.L.; He, Q.; Li, Z.H.; Yu, J.X.; Liu, X.C.; Ye, F.X. Corrosion products evolution and hot corrosion mechanisms of $REPO_4$ (RE= Gd, Nd, La) in the presence of $V_2O_5$ + $Na_2SO_4$ molten salt. *J. Eur. Ceram. Soc.* **2019**, *39*, 1496–1506. [CrossRef]
36. Guo, L.; Zhang, C.L.; Li, M.Z.; Sun, W.; Zhang, Z.Y.; Ye, F.X. Hot corrosion evaluation of $Gd_2O_3$-$Yb_2O_3$ co-doped $Y_2O_3$ stabilized $ZrO_2$ thermal barrier oxides exposed to $Na_2SO_4$+$V_2O_5$ molten salt. *Ceram. Int.* **2017**, *43*, 2780–2785. [CrossRef]
37. Guo, L.; Li, M.Z.; Ye, F.X. Phase stability and thermal conductivity of $RE_2O_3$ (RE=La, Nd, Gd, Yb) and $Yb_2O_3$ co-doped $Y_2O_3$ stabilized $ZrO_2$ ceramics. *Ceram. Int.* **2016**, *42*, 7360–7365. [CrossRef]
38. Hui, Y.; Zhao, S.M.; Xu, J.Y.; Zou, B.L.; Wang, Y.; Cai, X.L.; Zhu, L.; Cao, X.Q. High temperature corrosion behavior of zirconia ceramic in molten $Na_2SO_4$+$NaVO_3$ salt mixture. *Ceram. Int.* **2016**, *42*, 341–350. [CrossRef]
39. Zhang, Z.; Yang, Q.; Yu, Z.; Wang, H.; Zhang, T. Influence of Y2O3 addition on the microstructure of TiC reinforced Ti-based composite coating prepared by laser cladding. *Mater. Charact.* **2022**, *189*, 111962. [CrossRef]
40. Johns, R.L. Oxide acid-base reactions in ceramic corrosion. *High Temp. Sci.* **1989**, *27*, 369–380.

41. Jones, R.L. Scandia-stabilized zirconia for resistance to molten vanadate-sulfate corrosion. *Surf. Coat. Technol.* **1989**, *39–40*, 89–96. [CrossRef]
42. Xu, Z.H.; He, L.M.; Mu, R.D.; He, S.M.; Huang, G.H.; Cao, X.Q. Hot corrosion behavior of $La_2Zr_2O_7$ with the addition of $Y_2O_3$ thermal barrier coatings in contacts with vanadate-sulfate salts. *J. Alloys Compd.* **2010**, *504*, 382–385. [CrossRef]